RARE METALS

Doping induced morphology, crystal structure, and upconversion luminescence evolution: from Na$_3$ScF$_6$:Yb/Er/Y to NaYF$_4$:Yb/Er/Sc nanocrystals

Miao-Miao Liu, Guang-Chao Zheng, Yang Wei, Dan Tian, Qing-Bo Zheng, Ling Huang*[iD] , Juan Xie*[iD]

Abstract Impurity doping not only provides a fundamental approach to impart unique electronic, magnetic and optical properties to target nanomaterials, but also has critical influence on nucleation and growth of many functional nanocrystals. In the current study, Y^{3+} and Sc^{3+} were adopted to tune the shape, size, and upconversion luminescence properties of Na$_3$ScF$_6$:Yb/Er and NaYF$_4$:Yb/Er samples, respectively. When Y^{3+} doping concentration was lower than 10 mol%, the size and shape of Na$_3$ScF$_6$:Yb/Er (18/2) nanoparticles gradually changed from $\sim$ 18 nm rhombus to 36 nm spheres. Subsequently, the coexistence of Na$_3$ScF$_6$:Yb/Er and NaYF$_4$:Yb/Er nanoparticles was observed during 20 mol%–50 mol% Y^{3+} doping, and finally NaYF$_4$:Yb/Er nanoparticles became the only product at > 60 mol% Y^{3+} doping where the role of Sc^{3+} turned into dopant and the size of nanocrystals decreased from $\sim$ 30 to 20 nm gradually. Both Y^{3+} and Sc^{3+} ions doping could enhance the upconversion luminescence intensity of Na$_3$ScF$_6$:Yb/Er and NaYF$_4$:Yb/Er samples, for which possible mechanism was proposed from the perspective of crystal structure. Finally, the upconversion luminescence details were disclosed.

Keywords Doping; Crystal growth; Controlled synthesis; Upconversion

M.-M. Liu, G.-C. Zheng, Q.-B. Zheng, J. Xie*
School of Physics and Microelectronics, Zhengzhou University, Zhengzhou 450001, China
e-mail: juanxie@zzu.edu.cn

Y. Wei, L. Huang*
Key Laboratory of Flexible Electronics (KLOFE) and Institute of Advanced Materials (IAM), Jiangsu National Synergetic Innovation Center for Advanced Materials (SICAM), Nanjing Tech University (NanjingTech), Nanjing 211816, China
e-mail: iamlhuang@njtech.edu.cn

D. Tian
College of Materials Science and Engineering, Nanjing Forestry University, Nanjing 210037, China

1 Introduction

Rare-earth-based upconversion (UC) nanoparticles, enabling two or more low energy photons to convert into higher energy photons, have emerged as a unique kind of luminescent nanomaterials in the past decades [1–8]. The unique optical properties of UC nanoparticles, including high photostability, low background, fingerprint emission and tunable luminescent lifetime, make them promising candidates for sensing, anti-counterfeiting, and bioimaging [9–14]. Moreover, by integrating the luminescent features with other properties like magnetic properties, UC nanoparticles offer an opportunity to construct a multifunctional platform on a single particle for the rising theranostics [15–17].

Among various rare-earth-doped UC nanomaterials, Y-based fluorides are recognized as the most efficient ones for their wide band gap (> 10 eV), low phonon energy (350 cm^{-1}), good thermal stability and environmental safety [18–20], which can greatly minimize the non-irradiative relaxation during the photon UC process, thus acquiring higher efficient luminescence emission and having been widely used as both UC and even down-shifting host matrixes for various applications [21–26]. However, there is almost no study on the

impact of Y^{3+} ions acting as dopants on crystal structure and UC luminescence (UCL) properties of nanocrystals containing other rare-earth elements to the best of our knowledge.

Very recently, continuous efforts have been devoted to the scandium (Sc)-based luminescent nanomaterials, owing to the distinct electronic configuration of Sc^{3+} [27–31]. Notably, as the smallest rare-earth element, lanthanide-doped Sc-based compounds exhibit different optical behaviors compared with those of the rest, such as $NaYF_4$ nanomaterials. For example, $NaScF_4$:Yb/Er generates intensive red emission under 980 nm excitation, while $NaYF_4$:Yb/Er nanoparticles emit strong green light under identical conditions, induced by the different crystal structures of host materials and small ionic radii of Sc^{3+} [28, 32]. Moreover, by changing solvent polarity, hetero-structured Na_3ScF_6@$NaScF_4$ core-shell nanoparticles can be obtained, which indicates the potentiality for controlled synthesis of Sc-based UC nanoparticles [32]. Despite the advances in Sc-based nanomaterials, there are rare achievements on their size, morphology and crystal structure manipulation toward optical property tuning. In addition, it is still an urgent challenge to improve their luminescence efficiency. A variety of methods have been adopted to enhance the UC intensity, such as bringing in a co-dopant sensitizer [33, 34], constructing core-shell structures [35, 36], host lattice manipulation [37, 38], broadband sensitization [39], surface passivation and so on [40, 41]. Among these methods, introducing dopants into host lattice to change the lattice symmetry is useful to enhance UCL intensity. Moreover, due to the small ionic radius and the same valence, Sc^{3+} ions can also easily enter into the crystal lattices of other rare-earth-based nanomaterials as dopants for modulation of crystallographic parameters toward UCL tuning [42, 43].

Herein, we firstly introduced Y^{3+} as dopants into Na_3ScF_6:Yb/Er (18/2) system to tune the morphology, size, and UCL features. With the increasing of Y^{3+} concentration, hexagonal $NaYF_4$:Yb/Er nanoparticle became the only product while the Sc^{3+} began to act as dopants. For $NaYF_4$:Yb/Er/Sc (18/2/x mol%) systems, the variations of size, morphology and UCL intensity were also explored in detail. The crystal structure variation induced by doping from monoclinic Na_3ScF_6:Yb/Er to hexagonal $NaYF_4$:Yb/Er was carefully illustrated in Scheme 1. Then we obtained nanomaterials with strong red emission and green emission, respectively. The possible inherent mechanism for enhanced luminescence intensity was proposed. Such trivalent ions doping may give rise to interesting physical and chemical properties which are difficult to realize by mono- or bi-valent ions doping, such as Li^+ [44], Na^+ [45], or Zn^{2+}/Ca^{2+} [46–48].
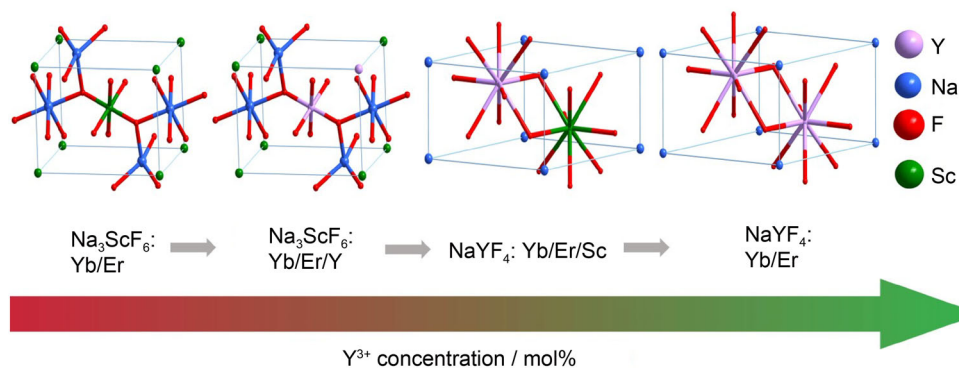
2 Experimental

2.1 Materials

Scandium (III) chloride hydrate (99.99 wt%), yttrium (III) chloride hydrate (99.99 wt%), erbium (III) chloride hydrate (99.99 wt%), ytterbium (III) chloride hydrate (99.99 wt%), sodium hydroxide (98 wt%), ammonium fluoride (98 wt%), methanol, cyclohexane, 1-octadecene (90 wt%) and oleic acid (90 wt%) were obtained from Sigma-Aldrich and used as received without further purification.

2.2 Characterization

Powder X-ray diffraction (XRD) analysis was carried out on a Bruker D8-advance diffractometer, operated at 40 kV and 40 mA with the monochromatized Cu Kα radiation (λ = 0.15406 nm) and the measurement was performed at ambient temperature in the range of 2θ = 10°–80° with 5 (°)·min^{-1}. Transmission electron microscopy (TEM) measurements were conducted on a Hitachi 7700 transmission electron microscope at an acceleration voltage of 100 kV. High resolution TEM (HRTEM) images and energy-dispersive X-ray (EDX) spectra were acquired on a Tecnai G2 F20 microscope. Elemental analysis of rare-earth ions was conducted by inductively coupled optical emission spectrometer (ICP-OES) analysis on a PE Optima 5300DV spectrometer. The UCL properties of Na_3Sc-F_6:Yb/Er/Y (18/2/x mol%) and $NaYF_4$:Yb/Er/Sc (18/2/x mol%) were characterized by Edinburgh F920 fluorescent spectrometer, which was equipped with a diode laser (980 nm). The pumping power of laser was fixed at a value of 20 mW for all samples.

2.3 Nanocrystals synthesis

In a typical experiment, 1 mmol RECl$_3$·6H$_2$O (x mol% Y, (80 − x) mol% Sc, 18 mol% Yb, 2 mol% Er) were added into a 50 ml three-necked flask containing oleic acid (12.5 ml) and 1-octadecene (12.5 ml) with magnetic stirring. The resulting mixture was heated to 150 °C and kept for 1 h under vigorous stirring before cooling down to 70 °C. Then, 10 ml methanol solution containing of 0.222 g NH$_4$F and 0.12 g NaOH was put into the flask. Subsequently, the resulting mixture was stirred for 30 min to remove the methanol, the solution was then heated to 300 °C under an N$_2$ environment for 1.5 h and cooled down to room temperature. Afterward, the reaction mixture was precipitated by addition of ethanol and collected by centrifugation for 5 min at 9000 r·min^{-1}. The as-synthesized nanocrystals were washed with ethanol and water for four times and finally redispersed in cyclohexane for future use.

Scheme 1 Schematic illustration of crystal structure evolution from monoclinic Na_3ScF_6:Yb/Er to hexagonal $NaYF_4$:Yb/Er nanocrystals at varying experimental conditions
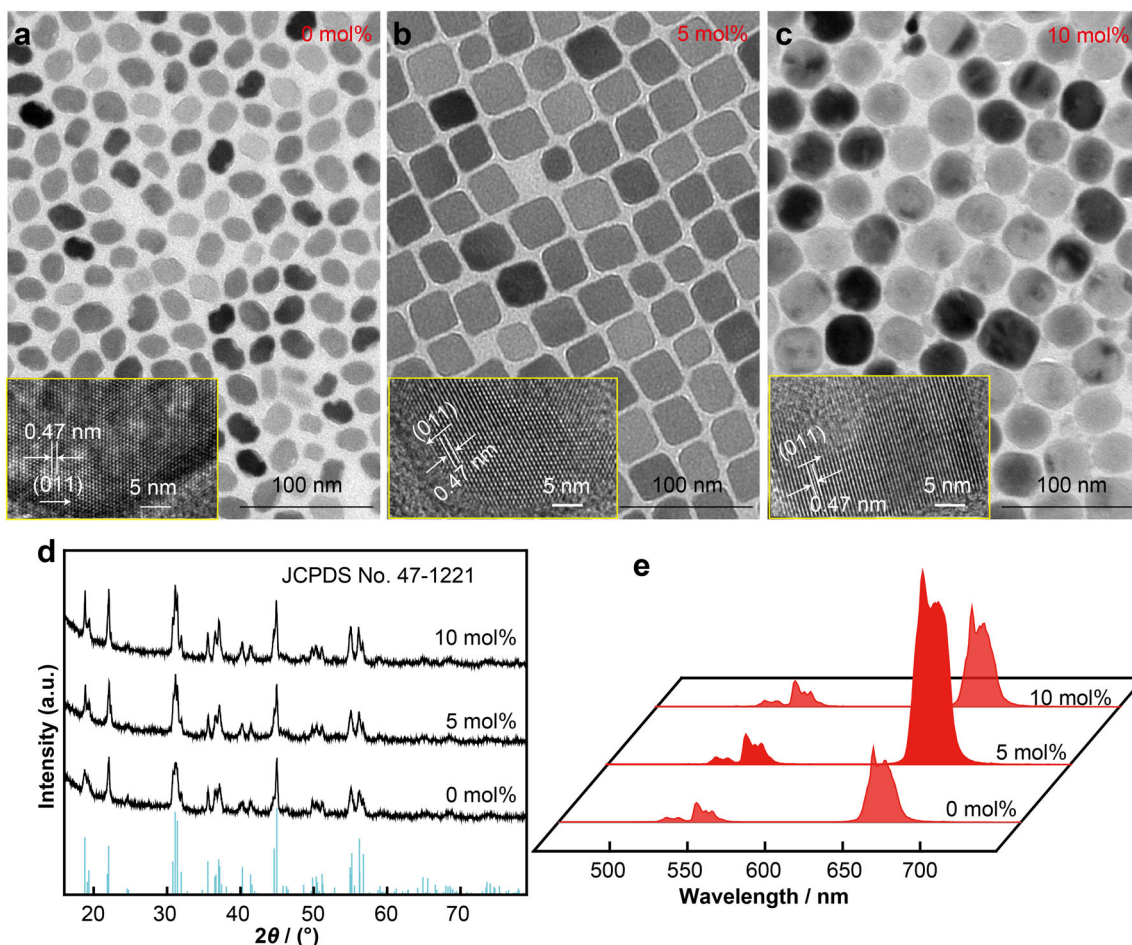

Fig. 1 **a–c** TEM images of Na_3ScF_6:Yb/Er/Y (18/2/x mol%) nanocrystals doped with 0 mol%, 5 mol% and 10 mol% Y^{3+}; insets in **a–c** are corresponding HRTEM images. **d** XRD patterns and **e** UCL spectra of samples in **a–c**

3 Results and discussion

TEM images shown in Fig. 1a–c indicate that the morphologies and sizes of as-synthesized Na_3ScF_6:Yb/Er/Y (18/2/x mol%) nanoparticles obviously change when Y^{3+}

doping concentration is increased. Rhombus-like Na_3Sc-F_6:Yb/Er (18/2 mol%) nanocrystals were obtained at 0 mol% Y^{3+} doping, of which the average size is ∼ 18 nm. Then the final products changed to cubes with the average size of ∼ 30 nm at 5 mol% Y^{3+} doping.

Nanospheres with average size of ~ 36 nm could be obtained if we kept increasing the doping concentration of Y^{3+} to 10 mol% (Fig. S1). XRD data in Fig. 1d indicate that the samples doping Y^{3+} ions at 0–10 mol% are all pure monoclinic phase Na_3ScF_6. The insets in Fig. 1a–c are HRTEM images of single Na_3ScF_6:Yb/Er/Y (18/2/x mol%) nanoparticles, indicating that the fringe distances are all ~ 0.47 nm and agree well with the lattice spacing of (011) planes of monoclinic Na_3ScF_6 crystals. Above results of XRD data and HRTEM analysis illustrate that introduction of Y^{3+} at 0–10 mol% did not alter the monoclinic single crystallinity of the final products and that Er^{3+}, Yb^{3+} and Y^{3+} were successfully doped into Na_3ScF_6 crystal lattices, as confirmed by elemental mapping (Figs. S2 and S3) and ICP-OES analysis (Table S1), where the actual Y^{3+} concentrations doped in Na_3ScF_6:Yb/Er/Y (18/2/x mol%) samples increase with the theoretical contents, though it is always lower than the feed value.

Under 980 nm laser excitation, the characteristic emission peaks of Er^{3+} centering at 545 and 654 nm (Fig. 1e) were observed for samples of Na_3ScF_6:Yb/Er/Y (18/2/x mol%, $x = 0$, 5, 10). The two emission bands could be ascribed to radiative energy transfer from $^2H_{11/2}$, $^4S_{3/2}$ and $^4F_{9/2}$ levels of Er^{3+} to its $^4I_{15/2}$ level, respectively. The emission focused on 654 nm was much stronger than that of 545 nm. Herein, stronger red UC emission were observed from all of Na_3ScF_6:Yb/Er/Y (18/2/x mol%, $x = 0$, 5, 10) samples, among which Na_3ScF_6:Yb/Er/Y (18/2/5 mol%) shows the strongest luminescence, Na_3ScF_6:Yb/Er/Y (18/2/10 mol%) ones are at the medium level, and Na_3ScF_6:Yb/Er (18/2 mol%) nanocrystals give the weakest. The intensity of Na_3ScF_6:Yb/Er/Y (18/2/5 mol%) sample is about 5 times as much as that of Na_3ScF_6:Yb/Er (18/2 mol%), which can be seen from Fig. S4a. Herein, Y^{3+} doping can effectively enhance the UCL intensity of Na_3ScF_6:Yb/Er (18/2 mol%) samples. It is worth pointing out that, though Y^{3+} introduction-induced particle size variation also gives rise to UCL enhancement because the surface defect density of corresponding sample reduces, it only takes up a very small portion because 10 mol% Y^{3+} doping nanocrystals own the largest size while the maximum enhancement is observed at 5 mol% Y^{3+} doping. Such comparison was carefully made by keeping other test conditions identical, which is helpful and straightforward to choose the most suitable one for further applications, such as biosensing, bioimaging and so on. The red to green ratio (R/G) also increases from 3.66 in Na_3ScF_6:Yb/Er (18/2 mol%) to 10.29 in Na_3ScF_6:Yb/Er/Y (18/2/5 mol%) and 4.88 in Na_3ScF_6:Yb/Er/Y (18/2/10 mol%) (Fig. S4b).

When Y^{3+} doping concentrations were set as 20 mol%–50 mol%, mixture was obtained. Corresponding TEM images, HRTEM images and XRD patterns are listed in Fig. 2. Small amount of nanospheres (Fig. 2a) which were recognized as hexagonal $NaYF_4$:Yb/Er according to XRD patterns (Fig. 2g), started to show up when Y^{3+} doping concentration was higher than 20 mol% though monoclinic Na_3ScF_6:Yb/Er nanocrystals were dominant. Then, the amount of hexagonal $NaYF_4$:Yb/Er samples kept increasing, which was accompanied with the decrease in monoclinic Na_3ScF_6:Yb/Er nanoparticles at increased Y^{3+} doping concentration until at 50 mol% Y^{3+} (Fig. 2g). Taking Na_3ScF_6:Yb/Er/Y (18/2/20 mol%) samples as an example, HRTEM images (Fig. 2e, f) corresponding to nanosphere and nanocubes selected from Fig. 2a show typical crystalline interplanar spacing of hexagonal $NaYF_4$ and monoclinic Na_3ScF_6, which were identified as 0.52 and 0.47 nm and matched well with (100) facet of hexagonal $NaYF_4$ crystals and (011) facet of monoclinic Na_3ScF_6, respectively. Herein, the two phased nanocrystals grew by themselves and existed as a physical mixture, rather than, for example, as core–shelled structures.

Further increasing Y^{3+} doping concentration to 60 mol%, monoclinic Na_3ScF_6 disappeared. TEM images, XRD patterns and UC luminescence spectra of pure hexagonal $NaYF_4$ nanocrystals are presented in Fig. 3. Uniform nanospheres were gained at 60 mol% Y^{3+} doping concentration (Fig. 3a), of which the average size was ~ 30 nm and XRD data indicated that monoclinic Na_3ScF_6:Yb/Er nanocrystals completely transformed into hexagonal $NaYF_4$:Yb/Er ones (Fig. 3e). Further increasing Y^{3+} concentration to 70 mol%, 75 mol% and even 80 mol% would not result in obvious morphology or phase structure variation of hexagonal $NaYF_4$:Yb/Er ones (Fig. 3b–e) though the sizes of final products kept decreasing. Figure S5 shows that the sizes of $NaYF_4$:Yb/Er/Sc (18/2/x mol%) samples with Y^{3+} concentrations of 70 mol%, 75 mol% and 80 mol% focus on 28, 24 and 22 nm, respectively. Compare the gradual variation of XRD patterns in Fig. 3e carefully, we found that diffraction peaks agree well with the standard hexagonal $NaYF_4$ (JCPDS No. 16-0334) and no impure diffraction peaks are seen at 60 mol%–80 mol% Y^{3+} doping concentration. Actually, hexagonal $NaYF_4$ became the host crystals while Sc^{3+} began to act as dopant and $NaYF_4$:Yb/Er/Sc nanospheres were the final products during this stage, as confirmed by elemental mapping (Figs. S6 and S7) and the ICP results (Table S2). Under 980 nm laser excitation, $NaYF_4$:Yb/Er/Sc (18/2/x mol%) nanocrystals all produce strong green UC emission (Fig. 3f), which is contrary to Na_3ScF_6:Yb/Er (18/2 mol%) nanoparticles generating strong red UC emission. The maximum UCL intensity enhancement of $NaYF_4$:Yb/Er/Sc (18/2/x mol%) samples was obtained at 75 mol% Y^{3+} contents, namely, i.e., at 5 mol% Sc^{3+} doping where ~ 10 times enhancement was observed. When the concentration of Y^{3+} was 80 mol% and no Sc^{3+} doping, the sample shows the lowest luminescence
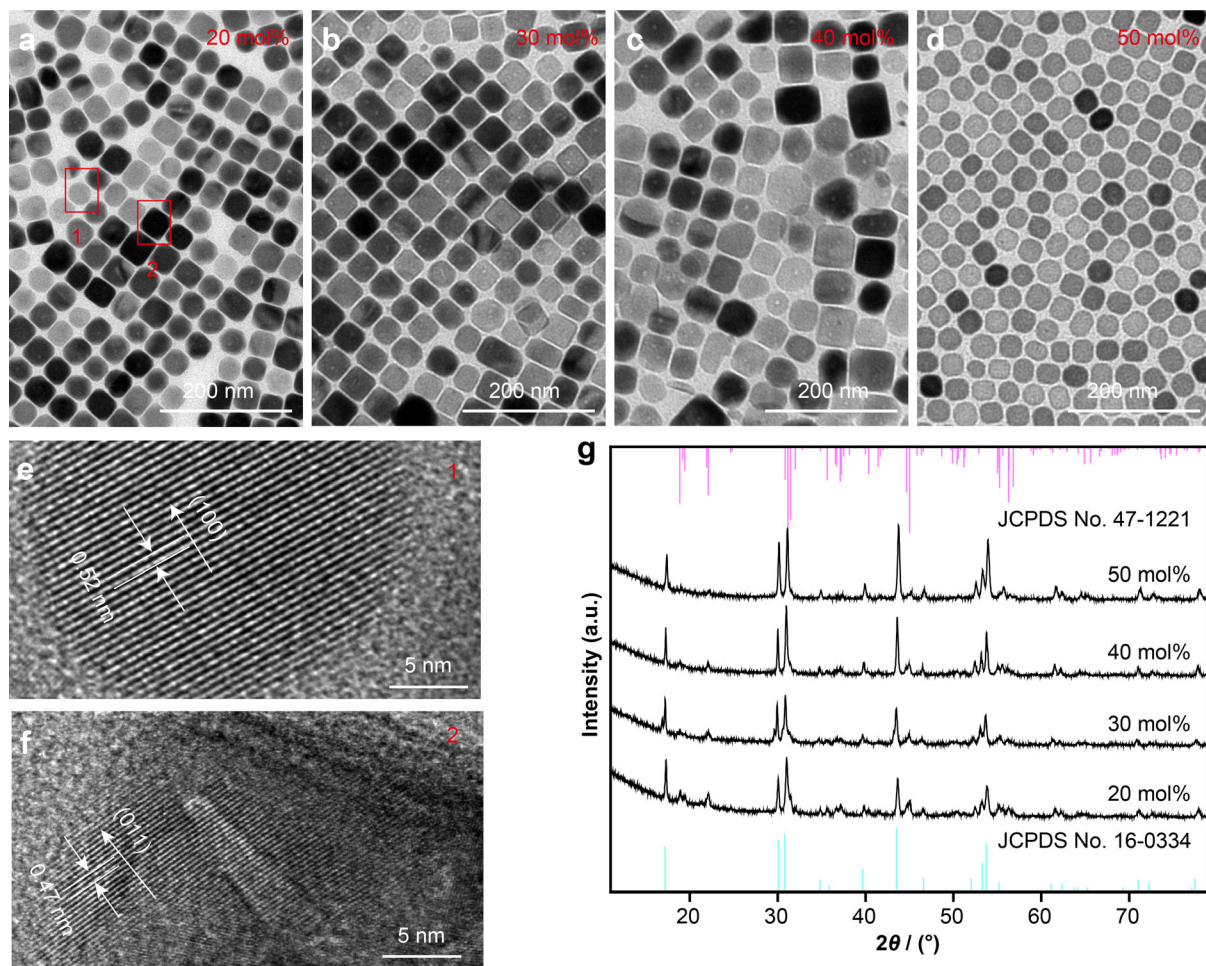
Fig. 2 Typical TEM images of Na₃ScF₆:Yb/Er/Y (18/2/x mol%) nanocrystals with Y^{3+} at **a** 20 mol%, **b** 30 mol%, **c** 40 mol%, **d** 50 mol% doping concentrations, respectively; **e**, **f** HRTEM images of nanocrystals selected from **a** showing hexagonal NaYF₄ and monoclinic Na₃ScF₆ crystal lattice constants, respectively; **g** XRD patterns of Na₃ScF₆:Yb/Er/Y (18/2/x mol%) nanocrystals

intensity, suggesting that introduction of Sc^{3+} into NaYF₄:Yb/Er (18/2) nanocrystals can also enhance UCL intensity. The integrated intensity of the samples can be directly observed from Fig. S8a. R/G ratio also varied with Y^{3+} contents increasing which is show in Fig. S8b.

According to the discussion above, we reason that the introduction of Y^{3+} or Sc^{3+} caused nanocrystal structures variation (expansion or contraction) takes responsibility for the UC emission enhancement. The introduction of dopants disturbed the local symmetry and resulted in changes in the crystal field. Consequently, the distance between sensitizer (Er^{3+}) and activator (Yb^{3+}) was affected, leading to energy transfer probabilities variation. Herein, UC emission intensity could be tuned [38]. To prove this viewpoint, we zoomed in the part of XRD patterns of Na₃ScF₆:Yb/Er/Y(18/2/x mol%) samples at 2θ of 20°–24°, finding that the positions of the diffraction peaks regularly shifted when Y^{3+} doping contents increased. As exhibited in Fig. 4a, the dominant diffraction peak at 22.038° which corresponds to

(110) crystal planes of monoclinic phase Na₃ScF₆:Yb/Er/Y (18/2/x mol%) samples gradually moves to smaller angle with Y^{3+} contents increasing from 0 to 10 mol%. For the situation of NaYF₄:Yb/Er/Sc (18/2/x mol%) samples, we pay attention to XRD patterns at 17.204° (Fig. 4b) which correspond to (100) facets of hexagonal phase NaYF₄ nanoparticles. Obviously, the diffraction peaks move to small angle during the range of 60 mol%–80 mol% Y^{+} concentrations. That is to say, the diffraction peaks of NaYF₄:Yb/Er/Sc (18/2/x mol%) nanocrystals shift gradually to larger angle with Sc^{3+} doping concentrations increasing. According to Bragg's Law:

$$n\lambda = 2d \sin \theta \tag{1}$$

where n is the order of reflection, λ is the wavelength of the incident wave (Cu Kα, 0.154 nm), d is the interplanar distance, and θ is the angle between the incident wave and the scattering planes. Herein, the enlarged interplanar crystal spacing will induce shifting toward a small
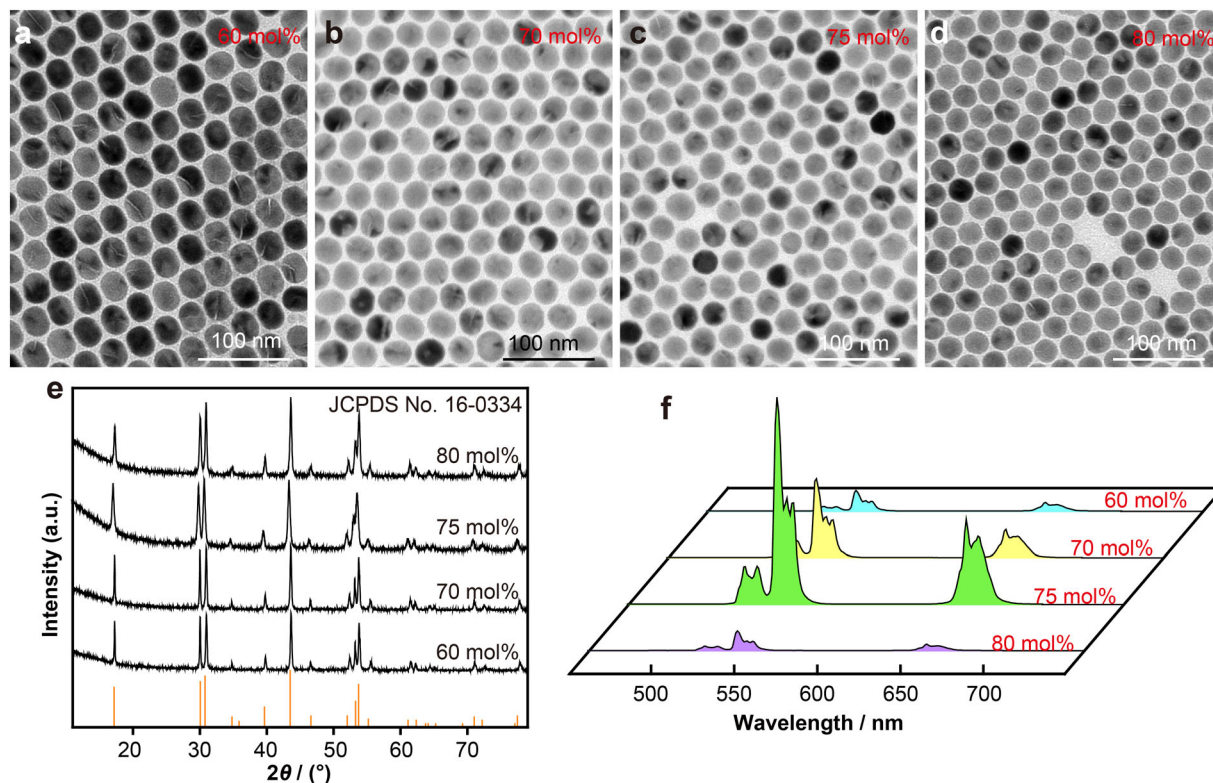
Fig. 3 TEM images of as-prepared NaYF$_4$:Yb/Er/Sc nanocrystals with Y^{3+} at **a** 60 mol%, **b** 70 mol%, **c** 75 mol%, **d** 80 mol% doping concentrations; **e** XRD patterns and **f** UC spectra of samples in **a–d**

diffraction angle, and vice versa. The effective ionic radius of Y^{3+} is 0.106 nm, which is close to that of Sc^{3+} (0.083 nm) [32]. Considering the same valence, it is easy for Y^{3+} and Sc^{3+} to substitute each other as dopants. For the Na$_3$ScF$_6$:Yb/Er/Y (18/2/x mol%) system, Y^{3+} with larger ionic radius act as dopants, which results in larger interplanar crystal spacing, i.e., smaller diffraction angle. This is consistent with XRD results (Fig. 4a). As to NaYF$_4$:Yb/Er/Sc (18/2/x mol%) nanoparticles, Sc^{3+} become dopants, the unit cell of NaYF$_4$ would shrink, making XRD peak shift toward bigger angles according to the Bragg's law, which agrees well with XRD patterns in Fig. 4b. Obviously, the introduction of dopants into host crystal structures will bring about changes in host lattice. Consequently, the local crystal field symmetry around emitters ions (Er^{3+}) was affected, which was anticipated to regulate their radiation parameters and enhance corresponding UCL intensity.

To explore the details of Y^{3+} or Sc^{3+} as dopants induced UCL enhancement, the excitation power-dependent UC emissions were characterized (Fig. 5). In general, during the unsaturated UC process, the photon numbers consumed for giving rise to an UC emission band can be described as the following equation:

$$I_{up} \propto P^n \tag{2}$$

where I_{up} represents the UCL intensity, P represents the pumping laser power and n represents the number of required pumping photons. Herein, the value of n can be acquired from the slope of the linear plots between lnI_{up} and ln$P$. For the case of Na$_3$ScF$_6$:Yb/Er/Y (18/2/x mol%), corresponding results are listed in Fig. 5a–c, which indicate that UC emissions fixing on 545 and 654 nm all abide by a two-photon process for the nanocrystals at Y^{3+} contents of 0 mol%, 5 mol% and 10 mol%, respectively. Figure S9a–d lists the photon numbers acquired for NaYF$_4$:Yb/Er/Sc nanocrystals with Y^{3+} contents at 60 mol%, 70 mol%, 75 mol% and 80 mol%. Also, both the green (545 nm) and red (654 nm) emissions follow two-photon UC processes no matter doping without or with Sc$^+$ at various contents. Herein, UC emission mechanism was not changed by Y^{3+} or Sc^{3+} doping. The outstanding variation in R/G ratios from Na$_3$ScF$_6$:Yb/Er/Y to NaYF$_4$:Yb/Er/Sc samples was due to difference in the host crystal structures and the ionic radii of Y^{3+} (0.106 nm) and Sc^{3+} (0.083 nm). On the one hand, the hexagonal NaYF$_4$ (JCPDS No. 16-0334) with the crystal lattice parameters of $a = b = 0.596$ nm and $c = 0.353$ nm tends to the energy transfer from $^4S_{3/2}$ and $^2H_{11/2}$ to $^4I_{15/2}$, generating obvious green UC luminescence, which is exhibited in Fig. 3f [26]. On the other hand, Sc^{3+}–Sc^{3+} distance is much shorter than

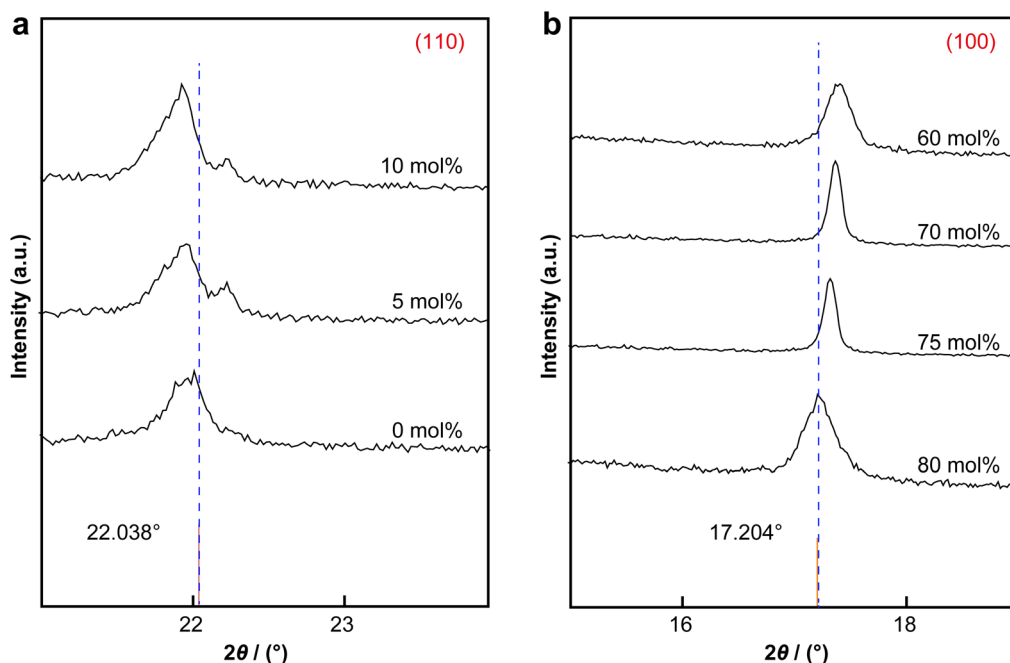**Fig. 4** **a** (110) crystal facet of monoclinic Na_3ScF_6:Yb/Er/Y (18/2/x mol%) doped with varying amounts of Y^{3+}; **b** (100) crystal facet of hexagonal $NaYF_4$:Yb/Er/Sc (18/2/x mol%) with various amounts of Y^{3+}

that of Y^{3+}–Y^{3+}, which will create closer Er^{3+}–Yb^{3+} cation pairs in Na_3ScF_6 system, which may result in much strong red emission [32].

Figure 5d depicts the energy level diagrams and UC processes of Er^{3+} and Yb^{3+} where Yb^{3+} was excited to the $^2F_{5/2}$ level by absorbing a 980 nm photon. The corresponding energy was transferred to $^4I_{11/2}$ level of nearby Er^{3+} and went back to its ground state. Population on the metastable $^4I_{11/2}$ level, Er^{3+} can either relax to its lower state $^4I_{13/2}$ through nonradiative transfer process or directly arrive at its higher energy level $^4F_{7/2}$ by absorbing another photon at 980 nm. From $^4I_{13/2}$ energy level, Er^{3+} can reach to its higher energy level $^4F_{9/2}$ by absorbing a 980 nm photon. Populating at $^4F_{7/2}$ state, Er^{3+} will emit 525 nm, 545 nm photons via relaxing to $^2H_{11/2}$ and $^4S_{3/2}$ level and then return to the ground state $^4I_{15/2}$. Meanwhile, the transitions from $^4F_{9/2}$ level to the ground state of Er^{3+} produce 654 nm photons.

As for the great difference in R/G ratio of monoclinic Na_3ScF_6:Yb/Er and hexagonal $NaYF_4$:Yb/Er, we speculate that the crystal structure of host material plays a crucial role. As the smallest rare-earth element whose ion radius was 0.083 nm (R_{Sc} = 0.083 nm), Sc-based materials may present shorter interatomic distances than other bigger rare-earth elements involved materials when present in the similar fluoride-bridged moieties inside the host lattice structure. Once Er^{3+} are introduced, they will occupy Sc sites. Consequently, red UC emission is realized for that relatively short Er^{3+}–Er^{3+} distance strengthen the cross-

relaxation between Er^{3+}, which promote the photon population on $^4F_{9/2}$ level of Er^{3+} (Fig. S10). Thus, monoclinic Na_3ScF_6:Yb/Er with relatively shorter Er^{3+}−Er^{3+} distance shows red UC luminescence and hexagonal $NaYF_4$:Yb/Er shows green UC luminescence [28, 32, 49, 50].

To further explore UC process and inherent mechanism, Er^{3+} decay curves for Na_3ScF_6:Yb/Er (18/2 mol%) and $NaYF_4$:Yb/Er (18/2 mol%) samples were characterized. The UCL lifetimes of Er^{3+} ions were recorded at 545 and 654 nm under 980 nm excitation, as shown in Fig. S11. Corresponding lifetime fitting parameters are presented in Table S3 and Table S4. The decay behaviors of Er^{3+} all show second-order exponential decay, which can be described by:

$$I(t) = A_1 \exp(-t/\tau_1) + A_2 \exp(-t/\tau_2) \qquad (3)$$

where I is the emission intensity, t is the time, τ_1 and τ_2 are the shorter and longer lifetime constants, and A_1, A_2 are fitting parameters which represent the original contributions for the shorter and longer decay time. Using these parameters, the average decay time can be determined by the following formula [51]:

$$\tau = \left(A_1\tau_1^2 + A_2\tau_2^2\right) + \left(A_1\tau_1 + A_2\tau_2\right) \qquad (4)$$

The lifetime values of $^4F_{9/2}$–$^4I_{15/2}$ and $^2H_{11/2}$/$^4S_{3/2}$–$^4I_{15/2}$ transitions for Er^{3+} were calculated in $NaYF_4$:Yb/Er and Na_3ScF_6:Yb/Er nanocrystals, respectively. As shown in Tables S3 and S4, the effective lifetime values of 545/654 nm were determined to be 445/864 and 95/148 μs in Na_3ScF_6:Yb/Er (18/2 mol%) and $NaYF_4$:Yb/Er (18/
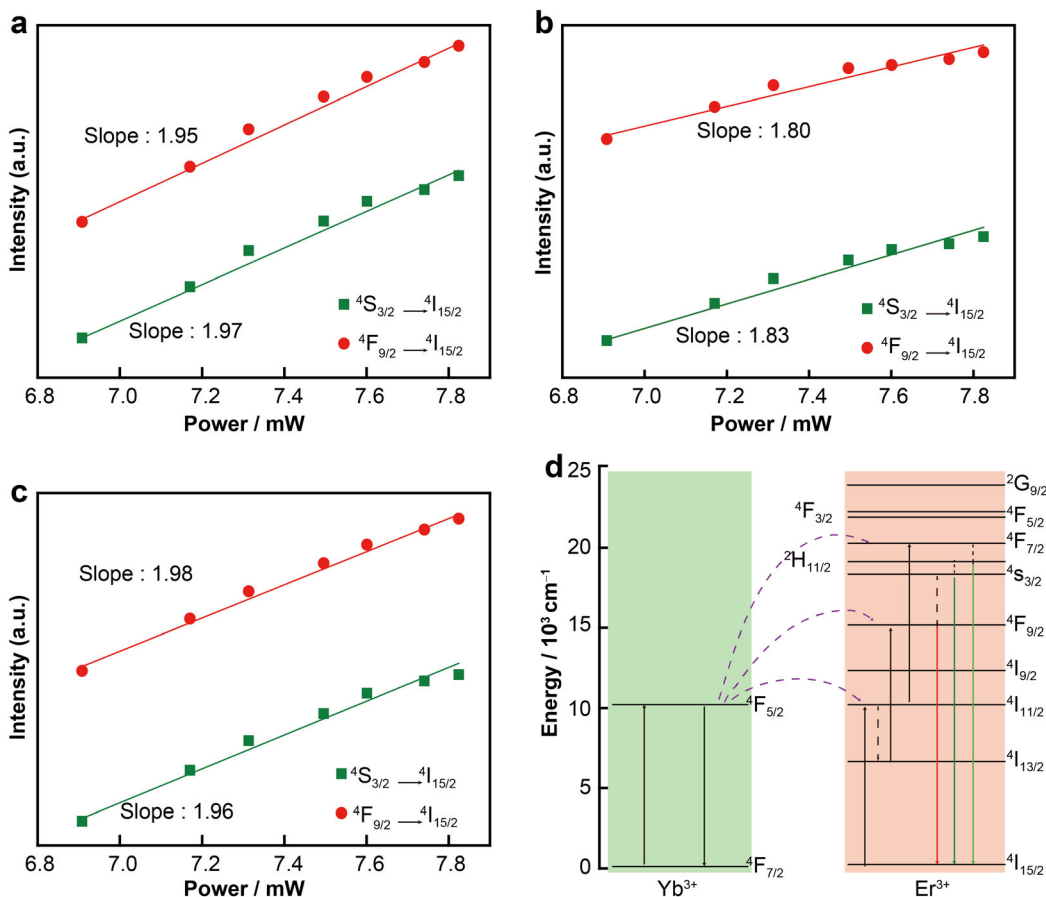
Fig. 5 a–c Pumping power dependence of green and red emission of Na_3ScF_6:Yb/Er/Y (18/2/x mol%) nanocrystals doped with 0 mol%, 5 mol% and 10 mol% of Y^{3+}; **d** schematic energy level diagrams of Yb^{3+} and Er^{3+} ions as well as proposed UC pathways for green and red emissions

2 mol%), respectively. As is well known, the lifetime constant is the reverse of the sum of the radiative and nonradiative transition rates. Compared with $NaYF_4$:Yb/Er nanocrystals, the shorter Yb^{3+}–Er^{3+} distance in Na_3ScF_6:Yb/Er enhances energy transfer from Yb^{3+} to Er^{3+}, which favors the phonon population of both $^4S_{3/2}/^2H_{11/2}$ and $^4F_{5/2}$ levels. Herein, it's reasonable that both the luminescence lifetimes of 545 and 654 nm are longer than that in $NaYF_4$:Yb/Er [49, 50]. By the way, for that the shorter Er^{3+}-Er^{3+} distance in Na_3ScF_6:Yb/Er also favor the cross-relaxation process ($^4F_{7/2}$ + $^4I_{11/2}$ − $^4F_{9/2}$ + $^4F_{9/2}$) of Er^{3+}, much more enhanced luminescence lifetime of 654 nm (from 148 to 864 μs) is observed compared with 545 nm (from 95 to 445 μs).

4 Conclusion

Precise-tuning of the crystal structure, size, morphology, and UCL of Na_3ScF_6:Yb/Er/Y and $NaYF_4$:Yb/Er/Sc has been realized through controlling Y^{3+} concentration, where ～ 5

and 10 times UCL enhancement was obtained in Na_3ScF_6:Yb/Er and $NaYF_4$:Yb/Er samples, respectively. Based on sufficient experimental details, the possible mechanism for enhanced luminescence intensity was proposed from the point view of nanocrystal structure. The current work has further disclosed the key function of Y^{3+} and Sc^{3+} in the controlled synthesis and property modulation of rare-earth-based UC nanocrystals and may pave a new way for us to select new materials with unique UCL property.

Declarations

Conflict of interests The authors declare that they have no conflict of interest.

References

[1] Ge H, Wang D, Pan Y, Guo Y, Li H, Zhang F, Zhu X, Li Y, Zhang C, Huang L. Sequence-dependent DNA functionalization

of upconversion nanoparticles and their programmable assemblies. Angew Chem Int Ed. 2020;59(21):8133. https://doi.org/10.1002/anie.202000831.

[2] Chen HW, Weng XY, Ma ZJ, Guan ZH. Microwave absorption properties of Mn-Zn ferrite with different Pr^{3+} content. Chin J Rare Met. 2020;44(12):1339. https://doi.org/10.13373/j.cnki.cjrm.XY19050029.

[3] Wen S, Zhou J, Schuck PJ, Suh YD, Schmidt TW, Jin D. Future and challenges for hybrid upconversion nanosystems. Nat Photonics. 2019;13(12):828. https://doi.org/10.1038/s41566-019-0528-x.

[4] Wu Y, Xu J, Poh ET, Liang L, Liu H, Yang JKW, Qiu C, Vallee RAL, Liu X. Upconversion superburst with sub-2 mus lifetime. Nat Nanotechnol. 2019;14(12):1110. https://doi.org/10.1038/s41565-019-0560-5.

[5] Zhong Y, Rostami I, Wang Z, Dai H, Hu Z. Energy migration engineering of bright rare-earth upconversion nanoparticles for excitation by light-emitting diodes. Adv Mater. 2015;27(41):6418. https://doi.org/10.1002/adma.201502272.

[6] Zhuo Z, Liu Y, Liu D, Huang P, Jiang F, Chen X, Hong M. Manipulating energy transfer in lanthanide-doped single nanoparticles for highly enhanced upconverting luminescence. Chem Sci. 2017;8(7):5050. https://doi.org/10.1039/C7SC01393K.

[7] Xie JH, Wang J, Qiu GH, Li XB, Huang WT, Zhang RR, Lin T, Wang LX, Zhang QT. A strategy to achieve efficient green-emission dual-mode luminescence of Yb^{3+}, Er^{3+} doped $NaBiF_4$. Rare Met. 2021;40(8):2040. https://doi.org/10.1007/s12598-020-01570-7.

[8] Li X, Ma H, Wang XD, Chen FF, Zeng XH. Structural and luminescent properties of Eu, Mg co-doped GaN. Chin J Rare Met. 2020;44(11):1170. https://doi.org/10.13373/j.cnki.cjrm.XY19040031.

[9] Li H, Tan M, Wang X, Li F, Zhang Y, Zhao L, Yang C, Chen G. Temporal multiplexed in vivo upconversion imaging. J Am Chem Soc. 2020;142(4):2023. https://doi.org/10.1021/jacs.9b11641.

[10] Kong MY, Gu YY, Liu YL, Shi YB, Wu N, Feng W, Li FY. Luminescence lifetime–based in vivo detection with responsive rare earth–dye nanocomposite. Small. 2019;15(46):1904487. https://doi.org/10.1002/smll.201904487.

[11] Wang J, Wei T, Li X, Zhang B, Wang J, Huang C, Yuan Q. Near-infrared-light-mediated imaging of latent fingerprints based on molecular recognition. Angew Chem Int Ed. 2014;53(6):1616. https://doi.org/10.1002/ange.201308843.

[12] Yi Z, Luo Z, Qin X, Chen Q, Liu X. Lanthanide-activated nanoparticles: a toolbox for bioimaging, therapeutics, and neuromodulation. Acc Chem Res. 2020;53(11):2692. https://doi.org/10.1021/acs.accounts.0c00513.

[13] Zhou L, Fan Y, Wang R, Li X, Fan L, Zhang F. High-capacity upconversion wavelength and lifetime binary encoding for multiplexed biodetection. Angew Chem Int Ed. 2018;57(39):12824. https://doi.org/10.1002/anie.201808209.

[14] Mahata MK, Koppe T, Kumar K, Hofsäss H, Vetter U. Upconversion photoluminescence of Ho^{3+}-Yb^{3+} doped barium titanate nanocrystallites: optical tools for structural phase detection and temperature probing. Sci Rep. 2020;10(1):8775. https://doi.org/10.1007/s12274-018-2159-9.

[15] Cong TD, Wang ZM, Hu M, Han QY, Xing BG. Extra-specific manifestation of nanoheater's position effect on distinctive cellular photothermal responses. ACS Nano. 2020;14(5):5836. https://doi.org/10.1021/acsnano.0c00951.

[16] Liu Y, Wang D, Shi J, Peng Q, Li Y. Magnetic tuning of upconversion luminescence in lanthanide-doped bifunctional nanocrystals. Angew Chem Int Ed. 2013;52(16):4366. https://doi.org/10.1002/ange.201209884.

[17] Lucky SS, Muhammad IN, Li Z, Huang K, Soo KC, Zhang Y. Titania coated upconversion nanoparticles for near-infrared light triggered photodynamic therapy. ACS Nano. 2015;9(1):191. https://doi.org/10.1021/nn503450t.

[18] Weber MJ. Probabilities for radiative and nonradiative decay of Er^{3+} in LaF_3. Phy Rev. 1967;157(2):262. https://doi.org/10.1103/physrev.157.262.

[19] Xie J, Gao Z, Zhou E, Cheng X, Wang Y, Xie X, Huang L, Huang W. Insights into the growth mechanism of REF_3 (RE = La-Lu, Y) nanocrystals: hexagonal and/or orthorhombic. Nanoscale. 2017;9(41):15974. https://doi.org/10.1039/C7NR06210A.

[20] Xie J, Hu W, Tian D, Wei Y, Zheng G, Huang L, Liang E. Selective growth and upconversion photoluminescence of Y--based fluorides: from $NaYF_4$:Yb/Er to YF_3:Yb/Er crystals. Nanotechnol. 2020;31(50):505605. https://doi.org/10.1088/1361-6528/abb627.

[21] Chen G, Qiu H, Prasad PN, Chen X. Upconversion nanoparticles: design, nanochemistry, and applications in theranostics. Chem Rev. 2014;114(10):5161. https://doi.org/10.1021/cr400425h.

[22] Gai S, Li C, Yang P, Lin J. Recent progress in rare earth micro/nanocrystals: soft chemical synthesis, luminescent properties, and biomedical applications. Chem Rev. 2014;114(4):2343. https://doi.org/10.1021/cr4001594.

[23] Gnach A, Lipinski T, Bednarkiewicz A, Rybka J, Capobianco JA. Upconverting nanoparticles: assessing the toxicity. Chem Soc Rev. 2015;44(6):1561. https://doi.org/10.1039/C4CS00177J.

[24] Fu R, Hu YY, Qiao HN, Yang CL, Yin H, Ou MG. Luminescence property and magnetic resonance imaging of Gd_2O_3:Tb^{3+} nanocrystals doped with Zn^{2+}, Li^+. Rare Met. 2021;40(8):2049. https://doi.org/10.1007/s12598-020-01591-2.

[25] Sun L, Wei R, Feng J, Zhang H. Tailored lanthanide-doped upconversion nanoparticles and their promising bioapplication prospects. Coord Chem Rev. 2018;364:10. https://doi.org/10.1016/j.ccr.2018.03.007.

[26] Zuo SL, Chen P, Pan CF. Mechanism of magnetic field-modulated luminescence from lanthanide ions in inorganic crystal: a review. Rare Met. 2020;39(10):1113. https://doi.org/10.1007/s12598-020-01450-0.

[27] Xie J, Zheng GC, Hu YM, Nosheen F, Zhang ZC, Liang EJ. Insight into crystal growth and upconversion luminescence property of tetragonal $Ba_3Sc_2F_{12}$ nanocrystals. Rare Met. 2021;40(1):113. https://doi.org/10.1007/s12598-020-01631-x.

[28] Ding Y, Teng X, Zhu H, Wang L, Pei W, Zhu JJ, Huang L, Huang W. Orthorhombic KSc_2F_7:Yb/Er nanorods:controlled synthesis and strong red upconversion emission. Nanoscale. 2013;5(23):11928. https://doi.org/10.1039/C3NR01840G.

[29] Pan Y, Xie X, Huang Q, Gao C, Wang Y, Wang L, Yang B, Su H, Huang L, Huang W. Inherently Eu^{2+}/Eu^{3+} codoped Sc_2O_3 nanoparticles as high-performance nanothermometers. Adv Mater. 2018;30(14):1705256. https://doi.org/10.1002/adma.201705256.

[30] Wang Y, Wen T, Zhang H, Sun J, Zhang M, Guo Y, Luo WJ, Xia MJ, Wang YX, Yang BC. Low-temperature fluorination route to lanthanide-doped monoclinic ScOF host material for tunable and nearly single band up-conversion luminescence. J Phys Chem C. 2014;118(19):10314. https://doi.org/10.1021/jp5020274.

[31] Xie J, Xie X, Mi C, Gao Z, Pan Y, Fan Q, Su HQ, Jin DY, Huang L, Huang W. Controlled synthesis, evolution mechanisms, and luminescent properties of ScF_x: Ln (x = 2.76, 3) nanocrystals. Chem Mater. 2017;29(22):9758. https://doi.org/10.1021/acs.chemmater.7b03561.

[32] Teng X, Zhu Y, Wei W, Wang S, Huang J, Naccache R, Hu W, Tok AIY, Han Y, Zhang QC, Fan QL, Huang W, Capobianco JA, Huang L. Lanthanide-doped Na_xScF_{3+x} nanocrystals: crystal structure evolution and multicolor tuning. J Am Chem Soc. 2012;134(20):8340. https://doi.org/10.1021/ja3016236.

[33] Peng D, Ju Q, Chen X, Ma R, Chen B, Bai G, Hao J, Qiao X, Fan X, Wang F. Lanthanide-doped energy cascade nanoparticles: full spectrum emission by single wavelength excitation. Chem Mater. 2015;27(8):3115. https://doi.org/10.1021/acs.chemmater.5b00775.

[34] Wang F, Liu X. Recent advances in the chemistry of lanthanide-doped upconversion nanocrystals. Chem Soc Rev. 2009;38(4):976. https://doi.org/10.1039/B809132N.

[35] Xie X, Gao N, Deng R, Sun Q, Xu QH, Liu X. Mechanistic investigation of photon upconversion in Nd^{3+}-sensitized core-shell nanoparticles. J Am Chem Soc. 2013;135(34):12608. https://doi.org/10.1021/ja4075002.

[36] Zuo J, Sun D, Tu L, Wu Y, Cao Y, Xue B, Zhang Y, Chang Y, Liu X, Kong X, Buma W, Meijer E, Zhang H. Precisely tailoring upconversion dynamics via energy migration in core-shell nanostructures. Angew Chem Int Ed. 2018;57(12):3054. https://doi.org/10.1002/anie.201711606.

[37] Hao D, Sun LD, Wang YF, Ke J, Si R, Xiao JW, Lyu G, Shi S, Yan CH. Efficient tailoring of upconversion selectivity by engineering local structure of lanthanides in Na_xREF_{3+x} nanocrystals. J Am Chem Soc. 2015;137(20):6569. https://doi.org/10.1021/jacs.5b01718.

[38] Han S, Deng R, Xie X, Liu X. Enhancing luminescence in lanthanide-doped upconversion nanoparticles. Angew Chem Int Ed. 2014;53(44):11702. https://doi.org/10.1002/anie.201403408.

[39] Zou W, Visser C, Maduro JA, Pshenichnikov MS, Hummelen JC. Broadband dye-sensitized upconversion of near-infrared light. Nat Photonics. 2012;6(8):560. https://doi.org/10.1038/nphoton.2012.158.

[40] Schäfer H, Ptacek P, Zerzouf O, Haase M. Synthesis and optical properties of KYF_4/Yb, Er nanocrystals, and their surface modification with undoped KYF_4. Adv Funct Mater. 2008;18(19):2913. https://doi.org/10.1002/adfm.200800368.

[41] Yi GS, Chow GW. Water-soluble $NaYF_4$:Yb, Er(Tm)/$NaYF_4$/ polymer core/shell/shell nanoparticles with significant enhancement of upconversion fluorescence. Chem Mater. 2007;19(3):341. https://doi.org/10.1021/cm062447y.

[42] He EJ, Chen SF, Zhang ML. Simultaneous morphology evolution and upconversion emission tuning of single Y-based fluoride microcrystal induced by Sc^{3+} co-doping. Mater Res Bull. 2017;87(Mar):61. https://doi.org/10.1016/j.materresbull.2016.11.025.

[43] Huang Q, Yu J, Ma E, Lin K. Synthesis and characterization of highly efficient near-infrared upconversion Sc^{3+}/Er^{3+}/Yb^{3+} tridoped $NaYF_4$. J Phys Chem C. 2010;114(10):4719. https://doi.org/10.1021/jp908645h.

[44] Wang Y, Wei T, Cheng X, Ma H, Pan Y, Xie J, Su H, Xie X, Huang L, Huang W. Insights into Li^+-induced morphology evolution and upconversion luminescence enhancement of KSc_2F_7:Yb/Er nanocrystals. J Mater Chem C. 2017;5(14):3503. https://doi.org/10.1039/C7TC00649G.

[45] Ding Y, Gu J, Ke J, Zhang YW, Yan CH. Sodium doping controlled synthesis of monodisperse lanthanide oxysulfide ultrathin nanoplates guided by density functional calculations. Angew Chem Int Ed. 2011;50(51):12330. https://doi.org/10.1002/ange.201105025.

[46] Lei L, Chen D, Huang P, Xu J, Zhang R, Wang Y. Modifying the size and uniformity of upconversion Yb/Er:$NaGdF_4$ nanocrystals through alkaline-earth doping. Nanoscale. 2013;5(22):11298. https://doi.org/10.1039/C3NR03497F.

[47] Liu X, Yi Z, Qin X, Liu H, Huang W, Liu X. Tuning long-lived Mn(II) upconversion luminescence through alkaline-earth metal doping and energy-level tailoring. Adv Opt Mater. 2019;7(15):1900519. https://doi.org/10.1002/adom.201900519.

[48] Mahata MK, Koppea T, Mondalb T, Brüsewitza C, Kumarb K, Raib V, Hofsässa H, Vettera U. Incorporation of Zn^{2+} ions into $BaTiO_3$:Er^{3+}/Yb^{3+} nanophosphor: an effective way to enhance upconversion, defect luminescence and temperature sensing. Phys Chem Chem Phys. 2015;17(32):20741. https://doi.org/10.1039/C5CP01874A.

[49] Cheng X, Ge H, Wei Y, Zhang K, Su W, Zhou J, Yin L, Zhan Q, Jing S, Huang L. Design for brighter photon upconversion emissions via energy level overlap of lanthanide ions. ACS Nano. 2018;12(11):10992. https://doi.org/10.1021/acsnano.8b04988.

[50] Huang F, Yang T, Wang S, Lin L, Tao Hud T, Chen D. Temperature sensitive cross relaxation between Er^{3+} ions in laminated hosts: a novel mechanism for thermochromic upconversion and high performance thermometry. J Mater Chem C. 2018;6(45):12364. https://doi.org/10.1039/C8TC04733B.

[51] Lakowicz JR. Principles of Fluorescence Spectroscopy. New York: Springer; 2010. 97. https://doi.org/10.1007/978-0-387-46312-4.